



OPEN Topological phases of extended Su-Schrieffer-Heeger-Hubbard model

Pei-Jie Chang¹, Jinghui Pi¹✉, Muxi Zheng¹, Yu-Ting Lei¹, Xingbo Pan¹, Dong Ruan^{1,2} & Gui-Lu Long^{1,2,3,4}✉

Despite extensive studies on the one-dimensional Su-Schrieffer-Heeger-Hubbard (SSH) model, the variant incorporating second-nearest neighbor hopping remains largely unexplored. Here, the topological classification of the extended SSH model is analyzed within the framework of the BDI symmetry class, using the winding number as the corresponding topological invariant. We investigate the ground-state properties of this extended SSH model using the constrained-path auxiliary-field quantum Monte Carlo (CP-AFQMC) method. We show that this model exhibits rich topological phases, characterized by robust edge states against interaction. We quantify the properties of these edge states by analyzing spin correlation and second-order Rényi entanglement entropy. The system exhibits long-range spin correlation and near-zero Rényi entropy at half-filling. Besides, there is an anti-ferromagnetic order at quarter-filling. Interestingly, an external magnetic field disrupts this anti-ferromagnetic order, restoring long-range spin correlation and near-zero Rényi entropy. Furthermore, our work provides a paradigm for studying topological properties in large interacting systems via the CP-AFQMC algorithm.

The topological phases of matter are a central topic in modern condensed matter physics due to their rich phenomenology and possible diverse applicability^{1–4}. This includes applications in topological spintronics^{5–7}, quantum metrology^{8–10}, and quantum computation^{11–13}. Within the independent electron approximation, topological matter can be characterized by topological band theory^{14–17}. Specifically, the degeneracy of zero-energy edge modes is directly associated with the topology of the bulk band through the bulk-edge correspondence^{18,19}. There are various experimental platforms to explore the topological states of matter, such as ultra-cold atoms^{20–22}, artificially engineered solid systems including graphene^{23,24}, arrays of carbon monoxide molecules^{25,26}, and exciton-polariton systems^{27,28}.

However, in many experimental setups, the interaction between electrons dominates the hopping amplitude^{29–32}, rendering the independent electron approximation invalid. The topological description of strongly correlated systems is an emerging area of research with significant potential^{33–42}. In interacting systems, the bulk-edge correspondence is modified as the relation between the bulk topological property and the many-body ground-state degeneracy on the edge^{43–46}. Researchers have also developed various metrics to evaluate and characterize topological edge states, including the Green function method^{47–50}, the entanglement entropy between topological edges and bulk states^{51–53}, and the topological phase transition induced by changes in magnetic flux^{54–56}. As a paradigmatic model for interacting topological systems, the Su-Schrieffer-Heeger (SSH) model with Hubbard interaction has been extensively studied^{57–64}. However, that incorporates second-nearest neighbor hopping remains largely unexplored.

Here, we discuss the ground-state properties of this extended interacting SSH model. In the absence of Hubbard interaction, the model can be well described by the single-particle theory and exhibits four distinct topological phases without breaking chiral symmetry^{65–69}. According to the bulk-edge correspondence, these topological phases are characterized by the number of zero-energy edge modes. In the presence of Hubbard interaction, we should consider the relation between the bulk topological property and the many-body ground state. We evaluate long-range spin correlation and the second-order Rényi entropy of the ground state, and determine the topological state of the system by measuring the correlation between the boundary and bulk. The presence of Hubbard interaction leads to a Mott gap at half-filling and dimerization at quarter-filling. To mitigate the influence of finite-site effects on our results, we employ the constrained-path auxiliary-field quantum Monte Carlo (CP-AFQMC) algorithm⁷⁰. Furthermore, the applicability of constrained-path method extends beyond the half-filling case⁵² where there is no sign problem. Our analysis reveals that the system exhibits long-range spin

¹State Key Laboratory of Low-Dimensional Quantum Physics and Department of Physics, Tsinghua University, Beijing 100084, China. ²Frontier Science Center for Quantum Information, Tsinghua University, Beijing 100084, China. ³Beijing Academy of Quantum Information Sciences, Beijing 100193, China. ⁴Beijing National Research Center for Information Science and Technology, Beijing 100084, China. ✉email: pijh14@gmail.com; gllong@tsinghua.edu.cn

correlation and near-zero Rényi entropy at half-filling, indicative of a topologically ordered state. Additionally, an antiferromagnetic order emerges at quarter-filling. The application of an external magnetic field disrupts this antiferromagnetic order, leading to a restoration of long-range spin correlation and near-zero Rényi entropy.

The rest of the paper is organized as follows. In Sec Model, we simulate the SSH model incorporating the second-nearest neighbor hopping. In Sec Result, we discuss the existence of long-range spin correlation and Rényi entanglement entropy at different fillings. In Sec Methods, we briefly review the exact diagonalization and CP-AFQMC methods. Summary and discussion are given in Sec Discussion. In the Supplementary Information, we give a result based on exact diagonalization as benchmark and a result of CP-AFQMC with different parameters.

Model

The extended interacting SSH model

Let us consider an interacting SSH model with second-nearest neighbor hopping. The Hamiltonian is given by

$$H = H_0 + H_U, \tag{1}$$

with hopping term

$$H_0 = - \sum_{i,\sigma} (J_{11} \hat{c}_{i,\sigma}^{A\dagger} \hat{c}_{i,\sigma}^B + J_1 \hat{c}_{i,\sigma}^{B\dagger} \hat{c}_{i+1,\sigma}^A + J_{33} \hat{c}_{i,\sigma}^{A\dagger} \hat{c}_{i+1,\sigma}^B + J_3 \hat{c}_{i,\sigma}^{B\dagger} \hat{c}_{i+2,\sigma}^A + h.c.), \tag{2}$$

and onsite Hubbard interaction term

$$H_U = \sum_{i,s} U \hat{n}_{i\uparrow}^s \hat{n}_{i\downarrow}^s, \tag{3}$$

where $\hat{c}_{i\sigma}^{s\dagger}$ is the fermion creation operator of the i -th site with sub-lattice label s and spin label σ . The parameters J_1 and J_{11} represent the nearest neighbor inter-cell and intra-cell hopping, respectively, while J_3 and J_{33} are the second-nearest neighbor hopping between sublattices A and B, as shown in Fig. 1a. The strength of the interaction on-site U is associated with the particle number operator $\hat{n}_{i\sigma}^s = \hat{c}_{i\sigma}^{s\dagger} \hat{c}_{i\sigma}^s$.

We first discuss the topological phases of the SSH model with second-nearest neighbor hopping. The Bloch Hamiltonian for this model is

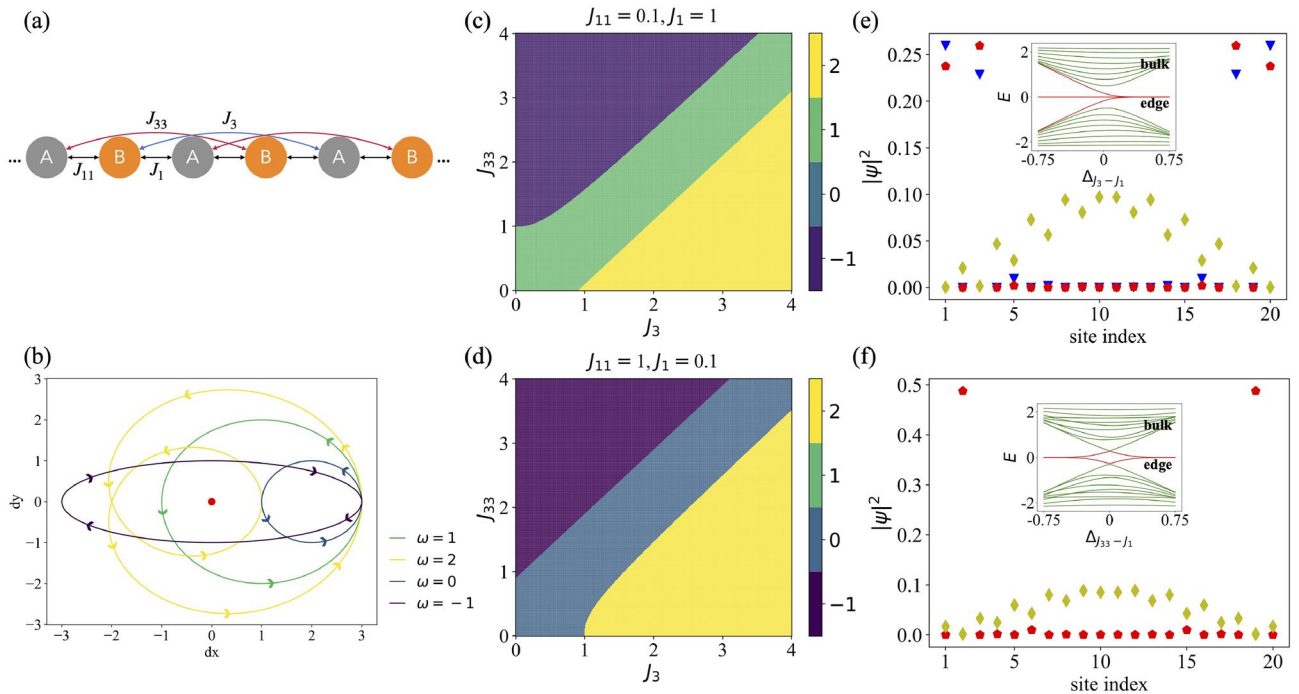


Fig. 1. The SSH model with second-nearest neighbor hopping. **(a)** Schematic diagram of hopping terms. **(b)** Wave function rotation in pseudo-spin space. The red point is the topological singular point and \mathcal{W} is corresponding winding number. Topological phase diagram by calculating \mathcal{W} with **(c)** $J_{11} = 0.1, J_1 = 1$, **(d)** $J_{11} = 1, J_1 = 0.1$. **(e), (f)** Particle distribution of a typical bulk state (diamond) and edge states (five-pointed star and inverted triangle) for $\Delta_{J_3(J_{33})-J_1} = 0.75$, which are along the $J_3(J_{33})$ axis in **(c)**, respectively. Inset: The corresponding energy spectrum for a 20-site chain. Here, we define that $\Delta_{J_3-J_1} = (J_3 - J_1)/2$, $\Delta_{J_{33}-J_1} = (J_{33} - J_1)/2$ and $\Delta_{J_{33}-J_{11}} = (J_{33} - J_{11})/2$.

$$\mathcal{H}(k) = d_x(k)\sigma_x + d_y(k)\sigma_y, \quad (4)$$

derived by the Fourier transform of H_0 under the periodic boundary condition. Here, $d_x = -J_{11} - (J_1 + J_{33}) \cos k - J_3 \cos 2k$ and $d_y = -J_{11} - (J_1 - J_{33}) \sin k - J_3 \sin 2k$, with $\sigma_{x(y)}$ denoting the Pauli matrices.

The model (4) exhibits a time-reversal symmetry \mathcal{T} , defined by $\mathcal{T}\mathcal{H}(k)\mathcal{T}^{-1} = \mathcal{H}(-k)$. This symmetry satisfies $\mathcal{T}^2 = 1$ and takes the form $\mathcal{T} = K$, where K is the complex conjugation operator. Additionally, the model preserves the chiral symmetry $\mathcal{C} = \sigma_z$, which is anti-commutative with the Hamiltonian, $\sigma_z\mathcal{H} = -\mathcal{H}\sigma_z$. Hence, each eigenstate $|\psi\rangle$ with energy E possesses a corresponding partner state $\sigma_z|\psi\rangle$ with energy $-E$. Furthermore, the model has particle-hole symmetry \mathcal{S} , which is a combination of time-reversal symmetry and chiral symmetry, $\mathcal{S} = \mathcal{T}\mathcal{C}$. This symmetry also anti-commutes with the Hamiltonian, $\mathcal{S}\mathcal{H} = -\mathcal{H}\mathcal{S}$. Thus, according to the classification of the tenfold way, this model belongs to the BDI topological class due to these three symmetries^{3,71}.

To characterize the topological property of the interaction-free model (4), we define the winding number \mathcal{W} as

$$\mathcal{W} = \frac{1}{2\pi} \int_{\text{FBZ}} \frac{d_x \partial_k d_y - d_y \partial_k d_x}{d_x^2 + d_y^2} dk, \quad (5)$$

where the integral is over the first Brillouin zone (FBZ), namely $k \in [0, 2\pi)$ as we set unit cell length $a = 1$. We plot the typical \mathcal{W} in the parameter space spanned by d_x and d_y in Fig. 1b. This winding number can be associated to the Zak phase^{54,72}

$$\gamma = i \int_{\text{FBZ}} \langle \psi | \partial_k | \psi \rangle dk \quad (6)$$

via $\gamma = \pi\mathcal{W}$, where $|\psi\rangle = \frac{1}{\sqrt{2}} \begin{pmatrix} \frac{d_x - id_y}{\sqrt{d_x^2 + d_y^2}} \\ -1 \end{pmatrix}^T$ is the normalized Bloch eigenstate with eigenvalue $\sqrt{d_x^2 + d_y^2}$. For $J_3 = J_{33} = 0$, the model reduces to the standard SSH model, which yields $\mathcal{W} = 0$ or 1, corresponding to topological trivial phase or topological non-trivial phase, respectively. When J_3 and J_{33} is non-zero, the phase diagram undergoes modifications that allow \mathcal{W} to take on additional values of -1 and 2, as shown in Fig. 1c and d.

According to the bulk-edge correspondence principle, the winding number \mathcal{W} defined by the bulk Hamiltonian (4) is directly related to the topological edge states under open boundary conditions. Specifically, $\mathcal{W} = 0$ implies that there are no topological edge states, while $\mathcal{W} = \pm 1$ leads to two zero-energy topological edge states at different sites. When $\mathcal{W} = 2$, the number of zero energy topological edge states increases to four. Fig. 1e illustrates the typical topological edge states at the 1_{st} , 3_{rd} , $(N-2)_{th}$, and N_{th} sites for $\mathcal{W} = 2$, while Fig. 1f shows the topological edge states at the 2_{nd} and $(N-1)_{th}$ sites for $\mathcal{W} = -1$.

In the presence of the Hubbard interaction ($U \neq 0$), the analytical solution of the model (1) via the Bethe ansatz becomes intractable in general⁷³. In the following part, we investigate the effect of U using numerical simulation techniques. For clarity, we briefly summarize the two numerical methods employed in this study.

Results

Edge population

In the absence of Hubbard interaction ($U = 0$), chiral symmetry ensures that eigenvalues appear in pairs ($E, -E$), leading to topological edge states at $E = 0$. As shown in Fig. 1e and f, while electrons gradually fill the bulk bands, they do not occupy the edge states until half-filling. The occupation of the edge state commences, as illustrated in Fig. 3a. Under the parameters in Fig. 3 (where $J_1 > J_{11}$), the outermost 1_{st} site and the N_{th} site always support the edge states. Therefore, varying $\Delta_{J_3-J_1}$ does not affect the filling of this specific pair of edge states.

The difference between the nearest neighbor hopping and the second-nearest hopping, $\Delta_{J_3-J_1}$ affects the topological properties of the 3_{rd} and $(N-2)_{th}$ sites according to Fig. 1c. When $\Delta_{J_3-J_1}$ is negative, these sites do not support edge states, resulting in a continuous variation of the electron population throughout the entire filling range, similar to bulk states. Conversely, for positive $\Delta_{J_3-J_1}$, a pair of edge states emerges at the 3_{rd} site and $(N-2)_{th}$ site, leading to a sharp change in electron population at half-filling, as illustrated by the transition from the blue to the red curve in Fig. 3b. When focusing on the filling behavior of the above four sites, we find that only all four sites support topological edge state does a sharp population change occur at half-filling, as shown in Fig. 3c.

In the strong interaction limit (large U), Coulomb repulsion between spin-up and spin-down electrons creates a Mott gap in the energy spectrum. This is reflected in the addition energy spectrum $E_{ad}(n) = E(n) - E(n-1)$, where n is the filling number of electrons. As expected for the Hubbard model, $E_{ad}(n)$ separates the lower and upper bands, as illustrated in Fig. 2a and b. In particular, when U is sufficiently large, the edge states begin to be filled with electrons at quarter-filling. When considering different electron fillings at this time, there will be a difference from no interaction, that is, electrons begin to occupy the edge state at quarter-filling ($n \text{ electrons} = 2$), as shown by the arrow in Fig. 3d-f. This discrepancy arises from the inherent gapless nature of symmetry-protected topological edge states. In a quarter-filled system with large U , introducing an additional

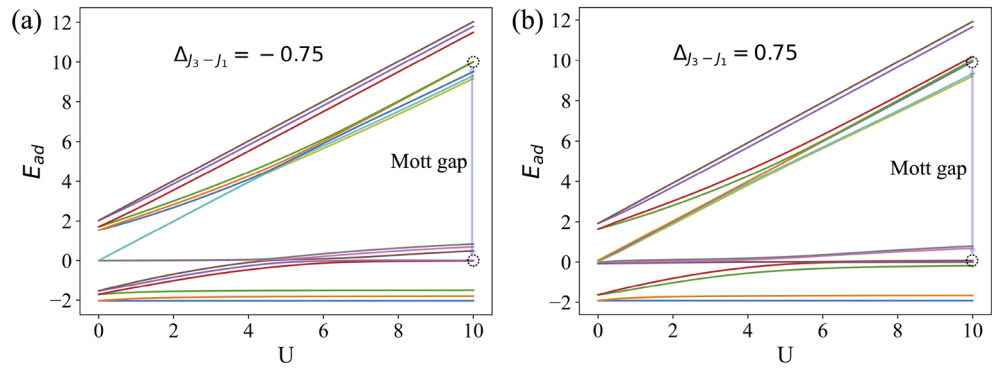


Fig. 2. The addition energy spectra of the extended interacting SSH model for a 8-site chain as a function of Hubbard U with $J_{11} = J_{33} = 0.1$ and (a) $\Delta_{J_3-J_1} = -0.75$, (b) $\Delta_{J_3-J_1} = 0.75$, respectively. Energy levels enclosed by dashed circles correspond to gapless states.

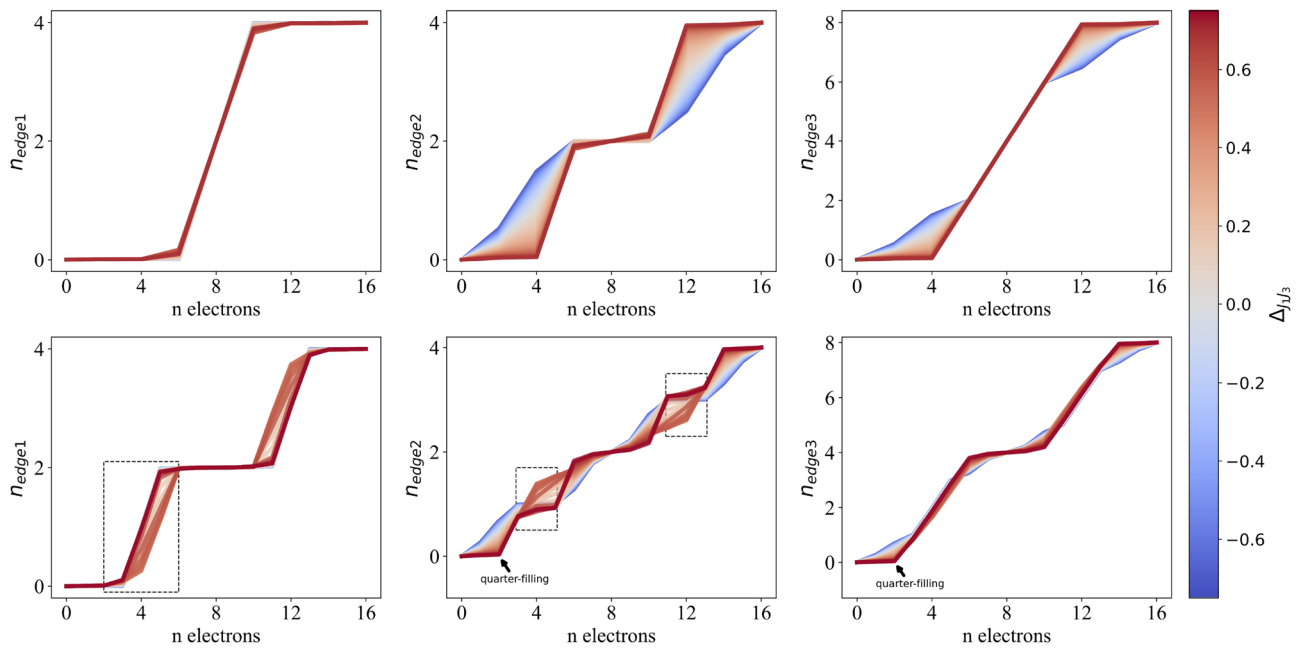


Fig. 3. The edge state population numbers for an 8-site chain with $J_{11} = J_{33} = 0.1$, and n is the number of electrons. (a)–(c) for $U = 0$ and (d)–(f) for $U = 10$. According to Fig. 1e, the edge states appear at the first boundary $[1_{st}, N_{th}]$ sites or the third-boundary $[3_{rd}, (N - 2)_{th}]$ sites. (a), (d) n_{edge1} are the total electron numbers on the 1_{st} and N_{th} sites, defined as $n_{edge1} = \langle \psi_0 | \hat{n}_1 + \hat{n}_N | \psi_0 \rangle$; (b), (e) Similarly, n_{edge2} is defined as $n_{edge2} = \langle \psi_0 | \hat{n}_3 + \hat{n}_{N-2} | \psi_0 \rangle$. (c), (f) n_{edge3} is the sum of n_{edge1} and n_{edge2} . The color indicates different values of $\Delta_{J_1 J_3}$. In the non-trivial phases without Hubbard U , the edge population increases sharply at half-filling. However, with Hubbard U , the edge population increases sharply at quarter-filling and three-quarter-filling. In the trivial phase, the edge population increases gradually. The wrinkle-like features enclosed by dashed boxes in (d)–(e) may be attributed to finite-size effects.

electron at any bulk site incurs a significant energy penalty due to the Hubbard interaction. In contrast, this additional electron can occupy the edge sites without energy cost.

Bulk-edge correspondence

The bulk-edge correspondence states that a system’s topological properties can be extracted by analyzing its edge states. The winding number, calculated under periodic boundary conditions, captures the topological nature of the bulk states. Well-defined boundaries enforced through open boundary conditions in simulations are necessary for the emergence of edge states. This correspondence dictates that a change in the winding number induces the appearance or disappearance of localized, gapless edge states that typically come in pairs.

As illustrated in Figs. 2 and 3, regardless of the presence or absence of strong interaction, the edge states of the half-filled system are always occupied by electrons.

We set $U = 10$, $J_{11} = J_{33} = 0.1$ to investigate the impact of $\Delta_{J_3-J_1}$ on the system (see Fig. 4). In this configuration, 1_{st} site and N_{th} site consistently support topological edge states as $J_1 > J_{11}$. Additionally, for $\Delta_{J_3-J_1} > 0$, the 3_{rd} and $(N-2)_{th}$ sites also support topological non-trivial edge states. These edge states are decoupled from the bulk and occur in pairs, which exist in a singlet state $|S\rangle = (|\uparrow\downarrow\rangle - |\downarrow\uparrow\rangle)/\sqrt{2}$ or one of the three triplet states: $|T_0\rangle = (|\uparrow\downarrow\rangle + |\downarrow\uparrow\rangle)/\sqrt{2}$, $|T_1\rangle = |\uparrow\uparrow\rangle$, and $|T_2\rangle = |\downarrow\downarrow\rangle$. All these states are zero-energy and gapless. When $\Delta_{J_3-J_1} < 0$, the half-filled ground state exhibits 4-fold degeneracy, which increases to 16 for $\Delta_{J_3-J_1} > 0$, as confirmed by exact diagonalization results in Supplementary Information. The presence of Hubbard interaction reduces the ground state degeneracy due to the exclusion principle, preventing the co-occupation of a single site by electrons with opposing spins, represented as $|\uparrow\downarrow\rangle_{site1} \otimes \emptyset_{site2}$.

Since edge states form either a decoupled single state or a triplet state, the topological properties of the bulk can be investigated by simulating spin correlation between different sites. We define the spin correlation $C_{j,k} = \langle S_{z,j} S_{z,k} \rangle$, where $S_{z,j} = \frac{1}{2}(\hat{n}_{j,\uparrow} - \hat{n}_{j,\downarrow})$ represents the spin operator of the z-component at site j . The spin correlation function can be calculated using the two-point correlation Green function, as detailed in Supplementary Information, based on Eq. (10) and Wick's theorem⁷⁴.

As the 1_{st} and N_{th} sites always support topological edge states, these sites are uncorrelated with the bulk sites, shown in Fig. 4a–c. When $\Delta_{J_3-J_1} > 0$, a long-range spin correlation arises between the 3_{rd} site and the $(N-2)_{th}$ site (see Fig. 4a), analogous to that between the 1_{st} site and the N_{th} site, as these sites also support topological non-trivial edge states. Conversely, when the 3_{rd} site and the $(N-2)_{th}$ site only support topological trivial states, long-range spin correlation is absent, and a long range anti-ferromagnetic order is observed in Fig. 4b. This finding is consistent with the Hubbard model's conclusion in the large U limit, which can be explained by second-order perturbation theory.

The long-range correlation effect can be observed not only through spin correlation but also by quantifying entanglement entropy. The appearance of paired topological edge states corresponds to a near-zero entanglement. Given that edge states are located at the system boundaries, the formation of these states can be assessed by calculating the long-range entanglement entropy between the edge sites and the bulk sites. Define the reduced density matrix of the subsystem A as $\rho_A = Tr_{\bar{A}}|\Psi\rangle\langle\Psi|$, where A consists of the 1_{st} site and the N_{th} site or the 3_{rd} site and the $(N-2)_{th}$ site. The Rényi entropy can be calculated using the reduced density matrix of the subsystem A as $S_n = -\frac{1}{n-1} \log_2[Tr(\rho_A^n)]$, where n is a positive integer representing the order of the

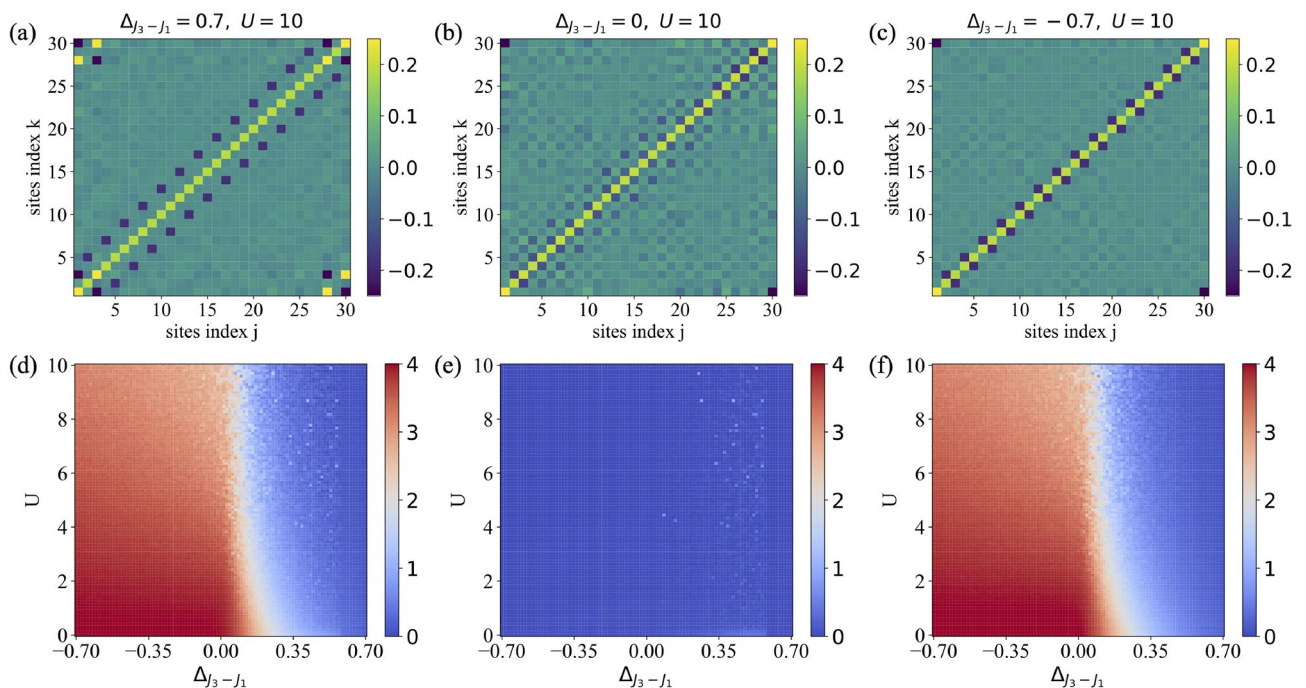


Fig. 4. CP-AFQMC results of the extended interacting SSH model at the half-filling, where $J_{11} = J_{33} = 0.1$. (a) Spin correlation $\langle S_{z,j} S_{z,k} \rangle$ with $\Delta_{J_3-J_1} = 0.7$, exhibiting topological edge states at the 1_{st} , 3_{rd} , $(N-2)_{th}$, and N_{th} sites. (b) Spin correlation with $\Delta_{J_3-J_1} = 0$, showing a long-range anti-ferromagnetic order. (c) Spin correlation with $\Delta_{J_3-J_1} = -0.7$, exhibiting topological edge states at the 1_{st} and N_{th} sites. (d)–(f) The Rényi entropy between subsystem A and the remaining part \bar{A} for different subsystem definitions: (d) $A = [3_{rd}, (N-2)_{th}]$ sites, (e) $A = [1_{st}, N_{th}]$ sites, and (f) $A = [1_{st}, 3_{rd}, (N-2)_{th}, N_{th}]$ sites. The transition point observed in (d)–(f) is closer to $\Delta_{J_3-J_1} = 0$ than ED's results in Supplementary Information, suggesting a reduced impact of finite-size effects.

Rényi entropy. The entanglement between the subsystems A and the remaining part \bar{A} can be quantified by this Rényi entropy. In CP-AFQMC, the second-order Rényi entropy can be efficiently computed through the Green's function under different auxiliary fields^{75,76}:

$$S_2 = -\log \left[\sum_{\{s\}, \{s'\}} P_s P_{s'} \{ \text{Det}(G_{s,A} G_{s',A} + m(1 - G_{s,A})(1 - G_{s',A})) \} \right] \quad (7)$$

where G_s is equal-time Green function, and $G_s^{ij} = \langle \hat{c}_j^\dagger \hat{c}_i \rangle$ with $\hat{c}_i = (\hat{c}_{i\uparrow}, \hat{c}_{i\downarrow})$.

The presence of topological edge states can be assessed by using the second-order Rényi entropy. When topological edge states exist, the entanglement between the sites hosting these states and the remaining system is significantly reduced, as shown in Fig. 4d–f. Since the 1_{st} site and the N_{th} site can always support topological edge states, they exhibit near-zero entanglement with the bulk, as depicted in Fig. 4e. In addition, when $\Delta_{J_3-J_1}$ is adjusted to allow the 3_{rd} and $(N-2)_{th}$ sites to support a pair of topological edge states, the entanglement entropy also decreases close to zero. In all other configurations, the entanglement entropy remains a non-zero value. In particular, the observed decrease in the entanglement entropy does not occur precisely at $\Delta_{J_3-J_1} = 0$ due to finite-size effects, which diminish as the system size increases. This observation aligns with the exact diagonalization results presented in the Supplementary Information. As the system sizes are larger calculated by CP-AFQMC, the position where the entanglement entropy decreases approaches $\Delta_{J_3-J_1} = 0$.

In Fig. 5, we show the calculation results for $J_3 = J_1 = 0.1$, which are in agreement with the conclusions of Fig. 4. When $\Delta_{J_{33}-J_{11}} < 0$, the 1_{st} , 2_{nd} , $(N-1)_{th}$ and N_{th} sites cannot support topological edge states. This is attributed to the stronger intra-cell hopping ($J_{11} > J_3$) favoring dimer-like states, which are not disrupted by second-nearest neighbor hopping when $J_{11} > J_{33}$. This explains the sequential emergence of dimers observed in Fig. 5c. Furthermore, the Rényi entropy between the two outermost dimers and the remaining dimers remains negligible, as depicted in the left panel of Fig. 5f. When $\Delta_{J_{33}-J_{11}} > 0$, the 2_{nd} and $(N-1)_{th}$ sites become topological edge states. This scenario, illustrated in Fig. 5a, exhibits long-range spin correlation, and the Rényi entropy between the 2_{nd} , $(N-1)_{th}$ sites and other sites approaches zero, as shown in Fig. 5d.

Magnetic-field-induced transition at quarter-filling

Since the edge states are not occupied by electrons at quarter filling, the system exhibits only an antiferromagnetic state (AFM) at this filling across all topological phases. For the system parameters corresponding to Fig. 6a and

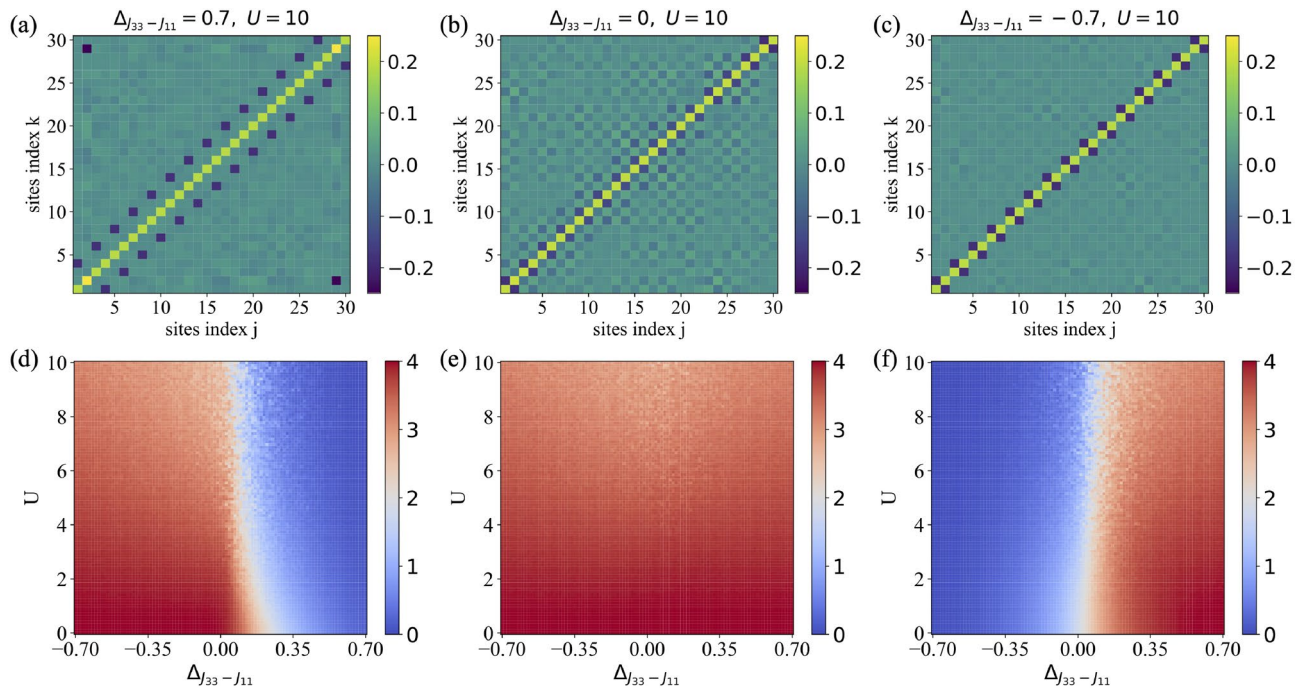


Fig. 5. CP-AFQMC results of the extended interacting SSH model at the half-filling, where $J_1 = J_3 = 0.1$. (a) Spin correlation $\langle S_{z,j} S_{z,k} \rangle$ with $\Delta_{J_{33}-J_{11}} = 0.7$, exhibiting topological edge states at the 2_{nd} and $(N-1)_{th}$ sites. (b) Spin correlation with $\Delta_{J_{33}-J_{11}} = 0.1$, showing a long-range anti-ferromagnetic order. (c) Spin correlation with $\Delta_{J_{33}-J_{11}} = -0.7$, and there are bulk dimers without topological edge states. (d) The Rényi entropy between subsystem $A = [2_{nd}, (N-1)_{th}]$ sites and the remaining part \bar{A} ; (Su-Schrieffer) The Rényi entropy with $A = [1_{st}, N_{th}]$ sites. (f) The Rényi entropy with $A = [1_{st}, 2_{nd}, (N-1)_{th}, N_{th}]$ sites. The formation of dimers leads to a decrease in Rényi entropy.

b, the sites where edge states appear are $[1_{st}, N_{th}]$ sites and $[1_{st}, 3_{rd}, (N - 2)_{th}, N_{th}]$ sites, respectively. The long-range spin correlation characteristic of half-filling is absent at quarter-filling. Instead, a long-range AFM order in Fig. 6a or a short-range AFM order in Fig. 6b characterized by adjacent or sub-adjacent spin correlation, is observed. This order, arising from the existence of an AFM order within the bulk, leads to a strong spin correlation between the edge states and the bulk. Consequently, the Rényi entropy does not drop significantly to zero when Δ_J changes along the axis with $E_B = 0$, as shown in Fig. 6c and d.

The Hamiltonian that describes the system under a magnetic field is given by $H_1 = H - (E_B/2)\sum_i(\hat{n}_{i\uparrow} - \hat{n}_{i\downarrow})$ with $E_B = g\mu_B B$, where μ_B is the Bohr magneton and g is the g -factor of the electron in the material. As discussed previously, the system exhibits no long-range spin correlation at quarter-filling in the absence of magnetic field. However, a sufficiently strong magnetic field can induce a transition to a maximally ferromagnetic ground state, as evidenced by the emergence of long-range spin correlation in Fig. 6c and d. This is attributed to the magnetic field effectively transforming the quarter-filling state into a quasi-half-filling state at high field strengths, resembling the true half-filling under zero magnetic field. Furthermore, the Rényi entropy will approach zero for $\Delta_J > 0$ due to the formation of new topological edge states. The contours depicted in Fig. 6c and d separate regions with distinct total spin S_z . For a one-dimensional chain with $N = 8$, a maximally ferromagnetic ground state at quarter-filling, with four spin-up electrons, corresponds to $S_z = 2$.

To achieve a maximally ferromagnetic state, the last spin-down electron needs to be pumped to the next unoccupied spin-up single-particle state. The presence of Hubbard interaction at quarter-filling raises the energy of only one spin-down electron compared to the $U = 0$ case. This lowers the critical magnetic field required to flip this spin-down electron to a spin-up state. Since it is very difficult to realize a strong magnetic field in experiments, the existence of Hubbard U enables the observation of this transformation under a much smaller magnetic field in experiments, as demonstrated in Fig. 6e and f.

Despite the sign problem at quarter-filling, we calculate the above results under different electron numbers using CP-AFQMC for a larger 1D chain with $N = 28$, as shown in Fig. 7. In the absence of a magnetic field, the particles do not occupy the topological edge states. However, as the magnetic field increases, the spins of the particles tend to align with the direction of the field. Due to the Pauli exclusion principle, particles with flipped spins occupy higher energy states. Once the magnetic field exceeds the critical value, the topological

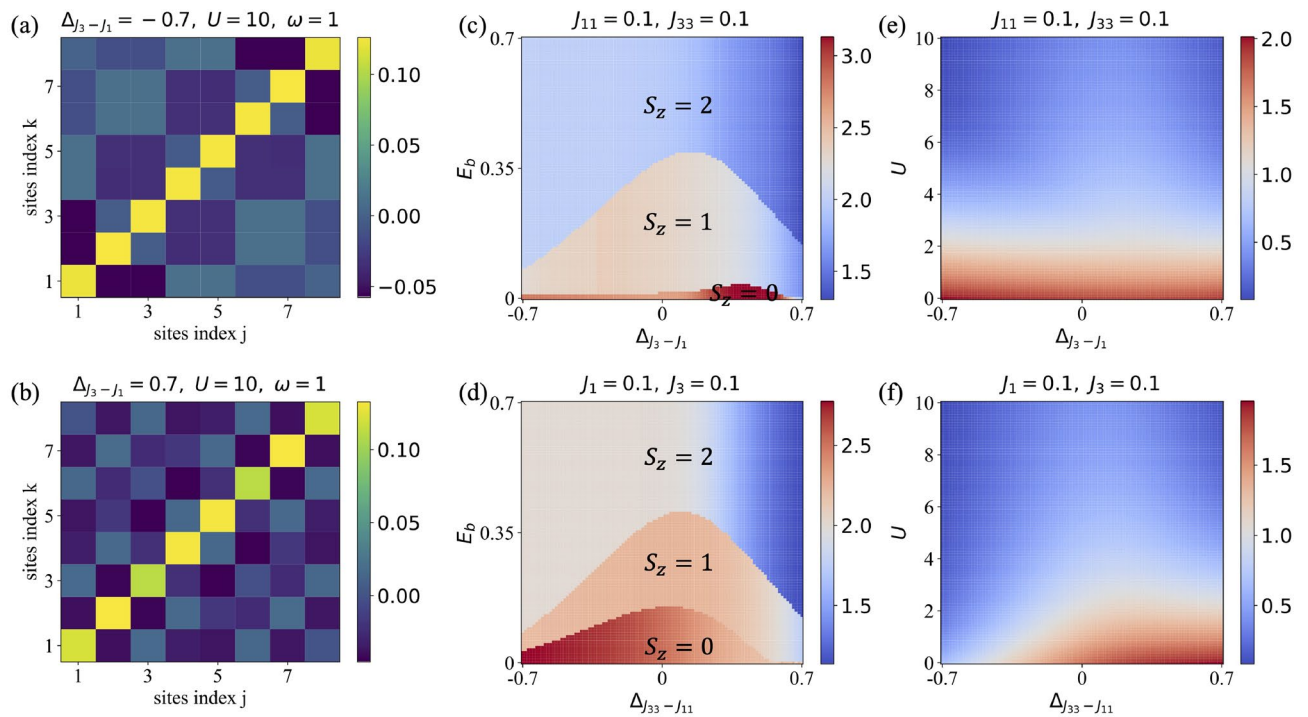


Fig. 6. ED's results of the extended interacting SSH model at the quarter-filling. **(a)** Spin correlation $\langle S_{z,j} S_{z,k} \rangle$ with $\Delta_{J_3-J_1} = -0.7$ and $J_{11} = J_{33} = 0.1$, topological edge states occupying the 1_{st} and N_{th} sites, and ω denoting the ground state degeneracy. **(b)** Spin correlation with $\Delta_{J_3-J_1} = 0.7$ and $J_{11} = J_{33} = 0.1$, topological edge states occupying the $1_{st}, (N - 2)_{th}, (N - 2)_{th}$ and N_{th} sites. **(c)** The Rényi entropy between the subsystem $A = [3_{rd}, (N - 2)_{th}]$ sites and the remaining part for varying field strength and $\Delta_{J_3-J_1}$. Each contour can separate with different spin-z component S_z , where $S_z = 2$ indicates the maximally ferromagnetic ground state and $S_z = 0$ indicates the paramagnetic ground state. **(d)** The Rényi entropy between the subsystem $A = [2_{nd}, (N - 1)_{th}]$ sites and the remaining part for varying field strength and $\Delta_{J_{33}-J_{11}}$. **(e)** Critical field strength for varying Hubbard U and $\Delta_{J_3-J_1}$. **(f)** Critical field strength for varying U and $\Delta_{J_{33}-J_{11}}$. For a 1D slice at $\Delta_{J_3-J_1} = const$ in **(e)** or $\Delta_{J_{33}-J_{11}} = const$ in **(f)**, the critical field decreases with increasing U .

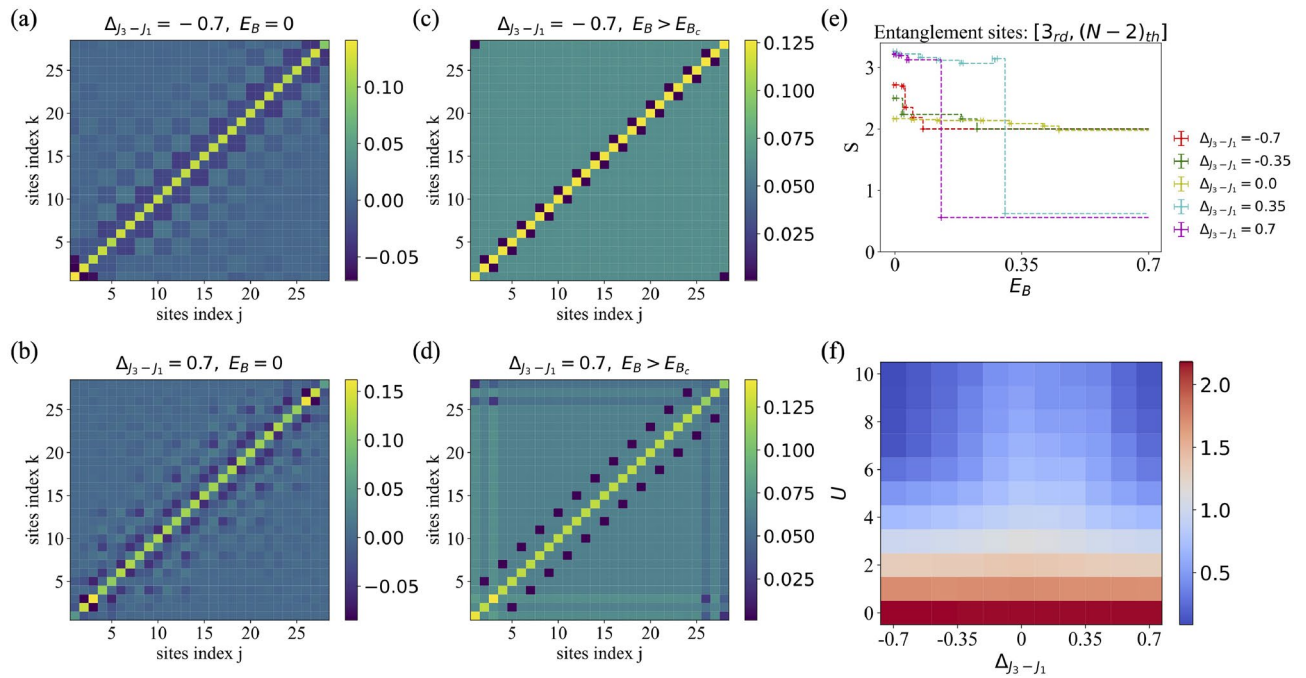


Fig. 7. CP-AFQMC results of the extended interacting SSH model at the quarter-filling with $J_{11} = J_{33} = 0.1$ and $U = 10$ for (a)–(e). (a) Spin correlation $\langle S_{z,j} S_{z,k} \rangle$ with $\Delta_{J_3-J_1} = -0.7$, topological edge states occupying the 1_{st} and N_{th} sites. (b) Spin correlation with $\Delta_{J_3-J_1} = 0.7$, topological edge states occupying the 1_{st} , 3_{rd} , $(N - 2)_{th}$, and N_{th} sites. (c), (d) Spin correlation $\langle S_{z,j} S_{z,k} \rangle$ above the critical magnetic field E_{B_c} , with $\Delta_{J_3-J_1} = -0.7$ in (c) and $\Delta_{J_3-J_1} = 0.7$ in (d). (e) The Rényi entropy with changing external magnetic field E_B and $\Delta_{J_3-J_1}$. Each point has errorbars of E_B and S , and the dotted line is a schematic line connecting different $\Delta_{J_3-J_1}$. (f) The critical field strength as a function of U and $\Delta_{J_3-J_1}$, revealing that for a given $\Delta_{J_3-J_1}$, the critical magnetic field decreases as U increases.

edge states become occupied. This indicates that the magnetic field introduces topological edge states component to the ground state at quarter-filling. However, the trial wave function at quarter-filling obtained from a single-particle model lacks an edge component. To address this, we propose a new trial wave function by linearly superimposing the single-particle wave function at quarter-filling with the topological edge states.

The combination is constructed as follows: $\psi_i = \frac{(\phi_i + \frac{1}{m} \sum_{j=1}^m f(\phi_i, \tilde{\phi}_j) * \tilde{\phi}_j)}{\sqrt{1+m}}$. Here, m denotes the number of

topological edge states, and $\tilde{\phi}_j$ represents the j_{th} edge state. The function $f(\phi_i, \tilde{\phi}_j)$ returns the sign (either $+1$ or -1) of the product $\tilde{\phi}_j[x] \times \phi_i[x]$, where x corresponds to the site position at which $\tilde{\phi}_j$ has its maximum probability amplitude. This new trial wave function can be used to reduce the system's bias at quarter-filling.

In Fig. 7a–d, we calculate the spin correlation, and the results are consistent with Fig. 6, that is, the long-range AFM order manifested under the critical magnetic field and the long-range spin correlation above the critical magnetic field. Subsequently, the Rényi entropy is calculated using formulas (7), as shown in Fig. 7e. For $\Delta_{J_3-J_1} < 0$, the entanglement entropy remains nonzero regardless of the applied magnetic field. Conversely, for $\Delta_{J_3-J_1} > 0$, the formation of long-range spin correlation leads to a decrease in entanglement entropy towards zero as the magnetic field strength increases. This behavior is consistent with Fig. 6c and d, where the entanglement entropy within each contour is a constant value. The calculated entanglement entropy for different spin configurations is connected by a polyline fit. The critical magnetic field, corresponding to the formation of the maximally ferromagnetic state, is defined as the magnetic field strength at which the entanglement entropy reaches its minimum for different values of $\Delta_{J_3-J_1}$. As illustrated in Fig. 7f, the relationship between the critical magnetic field and the Hubbard interaction is determined using CP-AFQMC. Similarly, a substantial decrease in the critical field is observed with increasing Hubbard interaction. The case $J_1 = J_3 = 0.1$ is detailed in the Supplementary Information.

Discussion

Topological edge states are a fundamental concept in topological physics, and their characterization is crucial for understanding the properties of topological materials. Spin correlation and entanglement entropy serve as essential measures for evaluating these edge states, even in strongly correlated systems.

In this work, we employ two computational techniques, ED and CP-AFQMC, to simulate the interacting SSH model incorporating second-nearest neighbor hopping. Through ED calculations, we observed that in small systems with Hubbard interaction, spin correlation, and Rényi entanglement entropy exhibit variations in

response to the relative magnitude of system hopping. To extrapolate to the thermodynamic limit, we utilize the CP-AFQMC algorithm and apply the method outlined in⁷⁵ to calculate the Rényi entanglement entropy of the system. The results obtained align with those from exact diagonalization but exhibit reduced finite-size effects.

When the system is at quarter-filling, antiferromagnetic (AFM) order emerges, leading to the disappearance of long-range spin correlation and a significant increase in entanglement entropy. Interestingly, if an external magnetic field is applied in this case, the system reverts to a quasi-half-filling state, reintroducing long-range spin correlation and reducing entanglement entropy to near zero.

During simulation at quarter-filling, the presence of a sign problem necessitates the use of the CP-AFQMC method to mitigate this issue. In this process, we utilize modified trial wave functions to achieve enhanced convergence. By calculating spin correlation and entanglement entropy using CP-AFQMC, we can extrapolate the results to other interacting topological systems, obtaining findings that closely approximate the thermodynamic limit.

Methods

Exact diagonalization

Exact diagonalization (ED) serves as a reference to solve quantum mechanics problems numerically. In theory, it provides a path to solve any problem given sufficient computational resources. However, condensed-matter lattice models often present exponentially difficult complexities. For example, the fermion Hubbard model scales as 4^N , where N represents the number of lattice sites. This rapid growth renders simulations of large-scale models computationally prohibitive. Despite these limitations, ED's accuracy and reliability make it valuable for obtaining reliable results in small-scale quantum simulations. We consider an open-boundary one-dimensional chain with $N = 8$ sites. The conserved particle number guarantees a $U(1)$ symmetry in the system. This symmetry allows for block diagonalization of the Hamiltonian, facilitating efficient diagonalization using the Lanczos algorithm. However, ED scales exponentially, restricting its application to small systems and inherently limiting studies of finite-size effects. To overcome this limitation and access the thermodynamic limit, we employ the CP-AFQMC method, detailed in the following section.

Constrained-path auxiliary-field quantum Monte Carlo

In this section, we give a brief introduction to CP-AFQMC, which is a powerful tool to solve the ground state problem in fermionic systems^{70,77–80}. Analogous to the power method for finding the dominant eigenvalue and eigenvector of a matrix⁸¹, iterative application of the imaginary time evolution operator to an initial state $|\psi_0\rangle$ recovers the ground state $|\psi_g\rangle$, provided the overlap is nonzero,

$$|\psi_g\rangle \propto \lim_{\beta \rightarrow \infty} e^{-\beta H} |\psi_0\rangle, \text{ if } \langle \psi_g | \psi_0 \rangle \neq 0. \quad (8)$$

To simplify numerical simulations, we assume that the initial state $|\psi_0\rangle$ is a single Slater determinant⁷⁹. In addition, since edge states come in degenerate pairs, constructing an appropriate $|\psi_0\rangle$ requires a suitable linear superposition of these states. For instance, if the single-particle edge states are $|\phi_1\rangle = (1, 0, \dots, 0)^T$, $|\phi_2\rangle = (0, \dots, 0, 1)^T$, the initial state $|\psi_0\rangle$ then can be chosen to $|\psi_1\rangle = (|\phi_1\rangle + |\phi_2\rangle)/\sqrt{2}$ or $|\psi_2\rangle = (|\phi_1\rangle - |\phi_2\rangle)/\sqrt{2}$.

Using Trotter decomposition, we can separate the imaginary time evolution process into single-body and multi-body contributions

$$e^{-\beta H} = (e^{-\frac{1}{2}\tau H_0} e^{-\tau H_U} e^{-\frac{1}{2}\tau H_0})^n + O(\tau^2), \quad (9)$$

where $\beta = \tau n$ represents the imaginary time length and τ denotes a single imaginary time step. In the calculation of AFQMC, a single-body operator applied to a Slater determinant can be efficiently computed, resulting in another Slater determinant. As two-body terms are incompatible with the Slater determinant formalism, the Hubbard-Stratonovich transformation is employed. By introducing an auxiliary field, this approach decouples the two-body term into a superposition of single-body terms⁸², facilitating efficient computations within Slater determinants. In AFQMC, the wave function is represented as a linear combination of Slater determinants (walkers). Eq. (8) is represented as random walks in the Slater determinant space by sampling the auxiliary fields.

A significant challenge in simulating quantum systems with the AFQMC method is the sign problem. This arises from negative weights assigned to certain configurations during the simulation, leading to a substantial increase in variance and consequently unreliable results. To address this challenge, the CP-AFQMC utilizes a trial wave function, denoted as $|\psi_T\rangle$. A key point is that walkers which have a negative overlap with the trial wave function are excluded, while those with significant overlap are replicated for propagation. Following extended imaginary-time evolution, the converged ground state energy and its associated wave function can be determined. A limitation of this method arises from the systematic errors introduced into the simulation results by the selection of $|\psi_T\rangle$. Optimizing $|\psi_T\rangle$ is an active research area within the CP-AFQMC framework^{83,84}. Here, we choose the initial state $|\psi_0\rangle$ as the trial wave function. Our primary focus is the characterization of edge states. Consequently, their existence or absence plays a crucial role in the simulations. This necessitates the implementation of a suitable linear superposition of $|\phi_1\rangle$ and $|\phi_2\rangle$, as previously established.

Physical quantities can be obtained using the equal-time Green's function, formulated as the mixed estimator,

$$G_{ij} = \langle \hat{c}_j^\dagger \hat{c}_i \rangle = \frac{\sum_k w_k \langle \psi_T | \hat{c}_j^\dagger \hat{c}_i | \psi_k \rangle}{\sum_k w_k \langle \psi_T | \psi_k \rangle}, \quad (10)$$

where $|\psi_k\rangle$ is the k_{th} walker, ω_k is the corresponding weight of the walker, and $|\psi_T\rangle$ is the trial wave function, identical to $|\psi_0\rangle$. Specifically, by employing Wick's theorem⁷⁴, physical observations like spin correlation and Rényi entanglement entropy can be calculated via the equal-time Green's function.

To benchmark CP-AFQMC calculations, exact diagonalization (ED) is performed on a 8-site chain. CP-AFQMC simulations are then conducted for a larger 30-site chain. The system exhibits no sign problem at half-filling, allowing us to employ parameters of $\tau = 0.05$, $N_{walker} = 100$, and $\beta = 15$, where τ is the time step for each imaginary-time evolution step, N_{walker} refers to the total number of walkers (samples) employed, and $\beta = n\tau$ denotes the total imaginary-time projection length. For systems away from half-filling, where a sign problem arises, we set $\tau = 0.01$, $N_{walker} = 2000$, and $\beta = 64$. Here, N_{walker} represents the number of walkers we use to perform a random walk.

Data availability

Pei-Jie Chang and Jinghui Pi have to be contacted in case of any queries or requirement of data. The datasets used and/or analysed during the current study available from the corresponding author on reasonable request.

Received: 17 February 2025; Accepted: 11 May 2025

Published online: 23 May 2025

References

- Hasan, M. Z. & Kane, C. L. Colloquium: Topological insulators. *Rev. Mod. Phys.* **82**, 3045–3067. <https://doi.org/10.1103/RevModPhys.82.3045> (2010).
- Qi, X.-L. & Zhang, S.-C. Topological insulators and superconductors. *Rev. Mod. Phys.* **83**, 1057–1110. <https://doi.org/10.1103/RevModPhys.83.1057> (2011).
- Chiu, C.-K., Teo, J. C. Y., Schnyder, A. P. & Ryu, S. Classification of topological quantum matter with symmetries. *Rev. Mod. Phys.* **88**, 035005. <https://doi.org/10.1103/RevModPhys.88.035005> (2016).
- Wen, X.-G. Colloquium: Zoo of quantum-topological phases of matter. *Rev. Mod. Phys.* **89**, 041004. <https://doi.org/10.1103/RevModPhys.89.041004> (2017).
- Nagaosa, N. & Tokura, Y. Topological properties and dynamics of magnetic skyrmions. *Nature Nanotechnol.* **8**, 899–911. <https://doi.org/10.1038/nnano.2013.243> (2013).
- Šmejkal, L., Mokrousov, Y., Yan, B. & MacDonald, A. H. Topological antiferromagnetic spintronics. *Nature Phys.* **14**, 242–251. <https://doi.org/10.1038/s41567-018-0064-5> (2018).
- Han, J. et al. Room-temperature spin-orbit torque switching induced by a topological insulator. *Phys. Rev. Lett.* **119**, 077702. <https://doi.org/10.1103/PhysRevLett.119.077702> (2017).
- Pekola, J. P. et al. Single-electron current sources: Toward a refined definition of the ampere. *Rev. Mod. Phys.* **85**, 1421. <https://doi.org/10.1103/RevModPhys.85.1421> (2013).
- Shen, Y. et al. Optical skyrmions and other topological quasiparticles of light. *Nature Photonics* **18**, 15–25. <https://doi.org/10.1038/s41566-023-01325-7> (2024).
- Peyruchat, L., Griesmar, J., Pillet, J.-D. & Girit, I. M. C. O. Transconductance quantization in a topological Josephson tunnel junction circuit. *Phys. Rev. Res.* **3**, 013289. <https://doi.org/10.1103/PhysRevResearch.3.013289> (2021).
- Beenakker, C. Search for Majorana fermions in superconductors. *Annu. Rev. Condens. Matter Phys.* **4**, 113–136. <https://doi.org/10.1146/annurev-conmatphys-030212-184337> (2013).
- Li, L., Xu, Z. & Chen, S. Topological phases of generalized Su-Schrieffer-Heeger models. *Phys. Rev. B* **89**, 085111. <https://doi.org/10.1103/PhysRevB.89.085111> (2014).
- Stern, A. & Lindner, N. H. Topological quantum computation—from basic concepts to first experiments. *Science* **339**, 1179–1184. <https://doi.org/10.1126/science.1231473> (2013).
- Fu, L., Kane, C. L. & Mele, E. J. Topological insulators in three dimensions. *Phys. Rev. Lett.* **98**, 106803. <https://doi.org/10.1103/PhysRevLett.98.106803> (2007).
- Hsieh, D. et al. A topological Dirac insulator in a quantum spin Hall phase. *Nature* **452**, 970–974. <https://doi.org/10.1038/nature06843> (2008).
- Zhang, H. et al. Topological insulators in Bi₂Se₃, Bi₂Te₃ and Sb₂Te₃ with a single Dirac cone on the surface. *Nature Phys.* **5**, 438–442. <https://doi.org/10.1038/nphys1270> (2009).
- Bansil, A., Lin, H. & Das, T. Colloquium: Topological band theory. *Rev. Mod. Phys.* **88**, 021004. <https://doi.org/10.1103/RevModPhys.88.021004> (2016).
- Ryu, S. & Hatsugai, Y. Topological origin of zero-energy edge states in particle-hole symmetric systems. *Phys. Rev. Lett.* **89**, 077002. <https://doi.org/10.1103/PhysRevLett.89.077002> (2002).
- Qi, X.-L., Wu, Y.-S. & Zhang, S.-C. General theorem relating the bulk topological number to edge states in two-dimensional insulators. *Phys. Rev. B* **74**, 045125. <https://doi.org/10.1103/PhysRevB.74.045125> (2006).
- Atala, M. et al. Direct measurement of the Zak phase in topological Bloch bands. *Nature Phys.* **9**, 795–800. <https://doi.org/10.1038/nphys2790> (2013).
- Cooper, N., Dalibard, J. & Spielman, I. Topological bands for ultracold atoms. *Rev. Mod. Phys.* **91**, 015005. <https://doi.org/10.1103/RevModPhys.91.015005> (2019).
- Zhang, J.-Y. et al. Tuning anomalous Floquet topological bands with ultracold atoms. *Phys. Rev. Lett.* **130**, 043201. <https://doi.org/10.1103/PhysRevLett.130.043201> (2023).
- Rizzo, D. J. et al. Topological band engineering of graphene nanoribbons. *Nature* **560**, 204–208. <https://doi.org/10.1038/s41586-018-0376-8> (2018).
- Pesin, D. & MacDonald, A. H. Spintronics and pseudospintronics in graphene and topological insulators. *Nature Mater.* **11**, 409–416. <https://doi.org/10.1038/nmat3305> (2012).
- Gomes, K. K., Mar, W., Ko, W., Guinea, F. & Manoharan, H. C. Designer Dirac fermions and topological phases in molecular graphene. *Nature* **483**, 306–310. <https://doi.org/10.1038/nature10941> (2012).
- Kempkes, S. et al. Robust zero-energy modes in an electronic higher-order topological insulator. *Nature Mater.* **18**, 1292–1297. <https://doi.org/10.1038/s41563-019-0483-4> (2019).
- Klemmt, S. et al. Exciton-polariton topological insulator. *Nature* **562**, 552–556. <https://doi.org/10.1038/s41586-018-0601-5> (2018).
- Su, R., Ghosh, S., Liew, T. C. & Xiong, Q. Optical switching of topological phase in a perovskite polariton lattice. *Sci. Adv.* **7**, eabf8049. <https://doi.org/10.1126/sciadv.abf8049> (2021).
- Le, N. H., Fisher, A. J. & Ginossar, E. Extended Hubbard model for mesoscopic transport in donor arrays in silicon. *Phys. Rev. B* **96**, 245406. <https://doi.org/10.1103/PhysRevB.96.245406> (2017).

30. Dusko, A., Delgado, A., Saraiva, A. & Koiller, B. Adequacy of si: P chains as fermi-hubbard simulators. *npj Quantum Inform.* **4**, 1. <https://doi.org/10.1038/s41534-017-0051-1> (2018).
31. Hu, H., Wang, J., Lalor, R. & Liu, X.-J. Two-dimensional coherent spectroscopy of trion-polaritons and exciton-polaritons in atomically thin transition metal dichalcogenides. *AAPPS Bull.* **33**, 12. <https://doi.org/10.1007/s43673-023-00081-8> (2023).
32. Kwan, Y. H., Ledwith, P. J., Lo, C. F. B. & Devakul, T. Strong-coupling topological states and phase transitions in helical trilayer graphene. *Phys. Rev. B* **109**, 125141. <https://doi.org/10.1103/PhysRevB.109.125141> (2024).
33. Rachel, S. Interacting topological insulators: A review. *Reports Progress Phys.* **81**, 116501. <https://doi.org/10.1088/1361-6633/aad6a6> (2018).
34. Jünemann, J. et al. Exploring interacting topological insulators with ultracold atoms: The synthetic creutz-hubbard model. *Phys. Rev. X* **7**, 031057. <https://doi.org/10.1103/PhysRevX.7.031057> (2017).
35. Nawa, K. et al. Triplon band splitting and topologically protected edge states in the dimerized antiferromagnet. *Nature Commun.* **10**, 2096. <https://doi.org/10.1038/s41467-019-10091-6> (2019).
36. Miao, J.-J., Jin, H.-K., Zhang, F.-C. & Zhou, Y. Exact solution for the interacting kitaev chain at the symmetric point. *Phys. Rev. Lett.* **118**, 267701. <https://doi.org/10.1103/PhysRevLett.118.267701> (2017).
37. Peri, V., Song, Z.-D., Bernevig, B. A. & Huber, S. D. Fragile topology and flat-band superconductivity in the strong-coupling regime. *Phys. Rev. Lett.* **126**, 027002. <https://doi.org/10.1103/PhysRevLett.126.027002> (2021).
38. Zhou, F. Topological quantum critical points in strong coupling limits: Global symmetries and strongly interacting majorana fermions. *Phys. Rev. B* **105**, 014503. <https://doi.org/10.1103/PhysRevB.105.014503> (2022).
39. Grusdt, F., Hönig, M. & Fleischhauer, M. Topological edge states in the one-dimensional superlattice bose-hubbard model. *Phys. Rev. Lett.* **110**, 260405. <https://doi.org/10.1103/PhysRevLett.110.260405> (2013).
40. Pan, H., Wu, F. & Das Sarma, S. Band topology, hubbard model, heisenberg model, and dzyaloshinskii-moriya interaction in twisted bilayer wse₂. *Phys. Rev. Res.* **2**, 033087. <https://doi.org/10.1103/PhysRevResearch.2.033087> (2020).
41. Meng, Z. Y., Hung, H.-H. & Lang, T. C. The characterization of topological properties in quantum Monte Carlo simulations of the kane-mele-hubbard model. *Modern Phys. Lett. B* **28**, 1430001. <https://doi.org/10.1142/S0217984914300014> (2014).
42. Bertok, E., Heidrich-Meisner, F. & Aligia, A. A. Splitting of topological charge pumping in an interacting two-component fermionic rice-mele hubbard model. *Phys. Rev. B* **106**, 045141. <https://doi.org/10.1103/PhysRevB.106.045141> (2022).
43. Tang, E. & Wen, X.-G. Interacting one-dimensional fermionic symmetry-protected topological phases. *Phys. Rev. Lett.* **109**, 096403. <https://doi.org/10.1103/PhysRevLett.109.096403> (2012).
44. Fraxanet, J. et al. Topological quantum critical points in the extended bose-hubbard model. *Phys. Rev. Lett.* **128**, 043402. <https://doi.org/10.1103/PhysRevLett.128.043402> (2022).
45. Kuno, Y. & Hatsugai, Y. Topological pump and bulk-edge-correspondence in an extended bose-hubbard model. *Phys. Rev. B* **104**, 125146. <https://doi.org/10.1103/PhysRevB.104.125146> (2021).
46. Mondal, S., Greschner, S., Santos, L. & Mishra, T. Topological inheritance in two-component hubbard models with single-component su-schrieffer-heeger dimerization. *Phys. Rev. A* **104**, 013315. <https://doi.org/10.1103/PhysRevA.104.013315> (2021).
47. Manmana, S. R., Essin, A. M., Noack, R. M. & Gurarie, V. Topological invariants and interacting one-dimensional fermionic systems. *Phys. Rev. B* **86**, 205119. <https://doi.org/10.1103/PhysRevB.86.205119> (2012).
48. Wagner, N. et al. Mott insulators with boundary zeros. *Nature Commun.* **14**, 7531. <https://doi.org/10.1038/s41467-023-42773-7> (2023).
49. Wagner, N., Guerci, D., Millis, A. J. & Sangiovanni, G. *Edge zeros and boundary spinons in topological mott insulators* **2312**, 13226 (2023).
50. Setty, C. et al. Electronic properties, correlated topology, and green's function zeros. *Phys. Rev. Res.* **6**, 033235. <https://doi.org/10.1103/PhysRevResearch.6.033235> (2024).
51. Jiang, H.-C., Wang, Z. & Balents, L. Identifying topological order by entanglement entropy. *Nature Phys.* **8**, 902–905. <https://doi.org/10.1038/nphys2465> (2012).
52. Jiang, D., Xu, S., Wang, Y. & Wu, C. Detecting edge degeneracy in interacting topological insulators through entanglement entropy. *Phys. Rev. B* **91**, 115118. <https://doi.org/10.1103/PhysRevB.91.115118> (2015).
53. Lee, C. H. Exceptional bound states and negative entanglement entropy. *Phys. Rev. Lett.* **128**, 010402. <https://doi.org/10.1103/PhysRevLett.128.010402> (2022).
54. Xiao, D., Chang, M.-C. & Niu, Q. Berry phase effects on electronic properties. *Rev. Mod. Phys.* **82**, 1959. <https://doi.org/10.1103/RevModPhys.82.1959> (2010).
55. De, S. J., Khanna, U. & Rao, S. Magnetic flux periodicity in second order topological superconductors. *Phys. Rev. B* **101**, 125429. <https://doi.org/10.1103/PhysRevB.101.125429> (2020).
56. Bhowmick, D. & Sengupta, P. Topological magnon bands in the flux state of shastry-sutherland lattice model. *Phys. Rev. B* **101**, 214403. <https://doi.org/10.1103/PhysRevB.101.214403> (2020).
57. Ahmadi, N., Abouie, J. & Baeriswyl, D. Topological and nontopological features of generalized su-schrieffer-heeger models. *Phys. Rev. B* **101**, 195117. <https://doi.org/10.1103/PhysRevB.101.195117> (2020).
58. Le, N. H., Fisher, A. J., Curson, N. J. & Ginossar, E. Topological phases of a dimerized fermi-hubbard model for semiconductor nano-lattices. *npj Quantum Inform.* **6**, 24. <https://doi.org/10.1038/s41534-020-0253-9> (2020).
59. Cai, X., Li, Z.-X. & Yao, H. Robustness of antiferromagnetism in the su-schrieffer-heeger hubbard model. *Phys. Rev. B* **106**, L081115. <https://doi.org/10.1103/PhysRevB.106.L081115> (2022).
60. Feng, C., Xing, B., Poletti, D., Scalettar, R. & Batrouni, G. Phase diagram of the su-schrieffer-heeger-hubbard model on a square lattice. *Phys. Rev. B* **106**, L081114. <https://doi.org/10.1103/PhysRevB.106.L081114> (2022).
61. Wang, H.-X., Jiang, Y.-F. & Yao, H. Robust d-wave superconductivity from the su-schrieffer-heeger-hubbard model: possible route to high-temperature superconductivity. <https://doi.org/10.48550/arXiv.2211.09143> (2022). 2211.09143.
62. Casebolt, M., Feng, C., Scalettar, R. T., Johnston, S. & Batrouni, G. G. Magnetic, charge, and bond order in the two-dimensional su-schrieffer-heeger-holstein model. *Phys. Rev. B* **110**, 045112. <https://doi.org/10.1103/PhysRevB.110.045112> (2024).
63. Chen, W., Peng, L., Lu, H. & Lu, X. Characterizing bulk-boundary correspondence of one-dimensional non-hermitian interacting systems by edge entanglement entropy. *Phys. Rev. B* **105**, 075126. <https://doi.org/10.1103/PhysRevB.105.075126> (2022).
64. Zhou, X., Pan, J.-S. & Jia, S. Exploring interacting topological insulator in the extended su-schrieffer-heeger model. *Phys. Rev. B* **107**, 054105. <https://doi.org/10.1103/PhysRevB.107.054105> (2023).
65. Pérez-González, B., Bello, M., Gómez-León, A. & Platero, G. Interplay between long-range hopping and disorder in topological systems. *Phys. Rev. B* **99**, 035146. <https://doi.org/10.1103/PhysRevB.99.035146> (2019).
66. Cinnirella, E. G., Nava, A., Campagnano, G. & Giuliano, D. Fate of high winding number topological phases in the disordered extended su-schrieffer-heeger model. *Phys. Rev. B* **109**, 035114. <https://doi.org/10.1103/PhysRevB.109.035114> (2024).
67. Dias, R. G. & Marques, A. M. Long-range hopping and indexing assumption in one-dimensional topological insulators. *Phys. Rev. B* **105**, 035102. <https://doi.org/10.1103/PhysRevB.105.035102> (2022).
68. Vega, C., Bello, M., Porras, D. & González-Tudela, A. Qubit-photon bound states in topological waveguides with long-range hoppings. *Phys. Rev. A* **104**, 053522. <https://doi.org/10.1103/PhysRevA.104.053522> (2021).
69. Kar, S. Edge state behavior in a su-schrieffer-heeger like model with periodically modulated hopping. *J. Phys. Condensed Matter* **36**, 065301. <https://doi.org/10.1088/1361-648X/ad0766> (2023).
70. Zhang, S., Carlson, J. & Gubernatis, J. E. Constrained path quantum Monte Carlo method for fermion ground states. *Phys. Rev. Lett.* **74**, 3652. <https://doi.org/10.1103/PhysRevLett.74.3652> (1995).

71. Ryu, S., Schnyder, A. P., Furusaki, A. & Ludwig, A. W. W. Topological insulators and superconductors: Tenfold way and dimensional hierarchy. *New J. Phys.* **12**, 065010. <https://doi.org/10.1088/1367-2630/12/6/065010> (2010).
72. Zak, J. Berry's phase for energy bands in solids. *Phys. Rev. Lett.* **62**, 2747–2750. <https://doi.org/10.1103/PhysRevLett.62.2747> (1989).
73. Bethe, H. On the theory of metals, i. eigenvalues and eigenfunctions of a linear chain of atoms. In *Selected Works Of Hans A Bethe: (With Commentary)*, 155–183, https://doi.org/10.1142/9789812795755_0004 (World Scientific, 1997).
74. Wick, G. C. The evaluation of the collision matrix. *Phys. Rev.* **80**, 268–272. <https://doi.org/10.1103/PhysRev.80.268> (1950).
75. Grover, T. Entanglement of interacting fermions in quantum Monte Carlo calculations. *Phys. Rev. Lett.* **111**, 130402. <https://doi.org/10.1103/PhysRevLett.111.130402> (2013).
76. Assaad, F. F., Lang, T. C. & Parisen Toldin, F. Entanglement spectra of interacting fermions in quantum Monte Carlo simulations. *Phys. Rev. B* **89**, 125121. <https://doi.org/10.1103/PhysRevB.89.125121> (2014).
77. Zhang, S., Carlson, J. & Gubernatis, J. E. Constrained path Monte Carlo method for fermion ground states. *Phys. Rev. B* **55**, 7464. <https://doi.org/10.1103/PhysRevB.55.7464> (1997).
78. Zhang, S. 15 Auxiliary-field quantum Monte Carlo for correlated electron systems. *Emergent Phenomena in Correlated Matter* <https://www.cond-mat.de/events/correl13/manuscripts> (2013).
79. Nguyen, H., Shi, H., Xu, J. & Zhang, S. Cpmc-lab: A matlab package for constrained path Monte Carlo calculations. *Comput. Phys. Commun.* **185**, 3344–3357. <https://doi.org/10.1016/j.cpc.2014.08.003> (2014).
80. He, Y.-Y., Qin, M., Shi, H., Lu, Z.-Y. & Zhang, S. Finite-temperature auxiliary-field quantum Monte Carlo: Self-consistent constraint and systematic approach to low temperatures. *Phys. Rev. B* **99**, 045108. <https://doi.org/10.1103/PhysRevB.99.045108> (2019).
81. Panza, M. J. Application of power method and dominant eigenvector/eigenvalue concept for approximate eigenspace solutions to mechanical engineering algebraic systems. *Am. J. Mechan. Eng.* **6**, 98–113. <https://doi.org/10.12691/ajme-6-3-3> (2018).
82. Hirsch, J. E. Discrete hubbard-stratonovich transformation for fermion lattice models. *Phys. Rev. B* **28**, 4059–4061. <https://doi.org/10.1103/PhysRevB.28.4059> (1983).
83. Qin, M. Self-consistent optimization of the trial wave function within the constrained path auxiliary field quantum Monte Carlo method using mixed estimators. *Phys. Rev. B* **107**, 235124. <https://doi.org/10.1103/PhysRevB.107.235124> (2023).
84. Vitali, E., Rosenberg, P. & Zhang, S. Calculating ground-state properties of correlated fermionic systems with bcs trial wave functions in slater determinant path-integral approaches. *Phys. Rev. A* **100**, 023621. <https://doi.org/10.1103/PhysRevA.100.023621> (2019).

Acknowledgements

The authors thank Yuhang Lu and Pengyu Wen for help with computing resources. The authors also thank Wenjia Rao, Shuai Chen, and Zhen Guo for their helpful discussion. This work is supported by the National Natural Science Foundation of China under Grants No. 11974205, and No. 61727801, the Key Research and Development Program of Guangdong province (2018B030325002), and National Natural Science Foundation of China under Grant 62131002.

Author contributions

Pei-Jie Chang completed the actual character research, program computation, data analysis, and visualization, as well as the drafting of the initial version of the article. Jinghui Pi proposed the idea, participated in the discussion of the algorithm for the article, and completed the review and revision of the article. Muxi Zheng refined the visualization effects of certain images and improved the algorithm. Yu-Ting Lei and Xingbo Pan revised the structure of the article and provided suggestions on its details. Dong Ruan and Gui-Lu Long provided financial support, supervised and led the work, and refined and polished the overall structure of the article.

Declarations

Competing interest

The authors did not report potential competing interest.

Additional information

Supplementary Information The online version contains supplementary material available at <https://doi.org/10.1038/s41598-025-02284-5>.

Correspondence and requests for materials should be addressed to J.P. or G.-L.L.

Reprints and permissions information is available at www.nature.com/reprints.

Publisher's note Springer Nature remains neutral with regard to jurisdictional claims in published maps and institutional affiliations.

Open Access This article is licensed under a Creative Commons Attribution-NonCommercial-NoDerivatives 4.0 International License, which permits any non-commercial use, sharing, distribution and reproduction in any medium or format, as long as you give appropriate credit to the original author(s) and the source, provide a link to the Creative Commons licence, and indicate if you modified the licensed material. You do not have permission under this licence to share adapted material derived from this article or parts of it. The images or other third party material in this article are included in the article's Creative Commons licence, unless indicated otherwise in a credit line to the material. If material is not included in the article's Creative Commons licence and your intended use is not permitted by statutory regulation or exceeds the permitted use, you will need to obtain permission directly from the copyright holder. To view a copy of this licence, visit <http://creativecommons.org/licenses/by-nc-nd/4.0/>.

© The Author(s) 2025